Probing Sodium Storage Mechanism in Hollow Carbon Nanospheres Using Liquid Phase Transmission Electron Microscopy

Jing Hou,* Zihan Song, Mateusz Odziomek, and Nadezda V. Tarakina*

Carbonaceous materials are promising sodium-ion battery anodes. Improving their performance requires a detailed understanding of the ion transport in these materials, some important aspects of which are still under debate. In this work, nitrogen-doped porous hollow carbon spheres (N-PHCSs) are employed as a model system for operando analysis of sodium storage behavior in a commercial liquid electrolyte at the nanoscale. By combining the ex situ characterization at different states of charge with operando transmission electron microscopy experiments, it is found that a solvated ionic layer forms on the surface of N-PHCSs at the beginning of sodiation, followed by the irreversible shell expansion due to the solid-electrolyte interphase (SEI) formation and subsequent storage of Na(0) within the porous carbon shell. This shows that binding between Na(0) and C creates a Schottky junction making Na deposition inside the spheres more energetically favorable at low current densities. During sodiation, the SEI fills the gap between N-PHCSs, binding spheres together and facilitating the sodium ions' transport toward the current collector and subsequent plating underneath the electrode. The N-PHCSs layer acts as a protective layer between the electrolyte and the current collector, suppressing the possible growth of dendrites at the anode.

1. Introduction

In view of global strategies to reduce carbon emissions, the energy paradigm is shifting towards using renewable energy sources (e.g., solar, wind) coupled with new generations of electrochemical storage devices. Lithium-ion batteries (LIBs) are the most mature energy storage technology so far, dominating the portable electronics and electric vehicles market in the last 30 years.[1] However, the high cost of lithium due to its limited natural abundance is accelerating the development of rechargeable batteries based on other earth-abundant elements.[2–4] Sodium's high availability, low cost, and apparent resemblance in electrochemistry to the established LIBs have made sodium-ion batteries (SIBs) one of the most promising solutions for the next generation of energy storage devices.[5–7] Even though sodium and lithium have similar physicochemical properties, including their one-electron valence shell and close standard electrode potential (Li/Li$^+$ = −3.04 V vs SHE, Na/Na$^+$ = −2.70 V vs SHE), the heavier atomic mass of sodium (22.99 g mol^{-1}) compared to lithium (6.94 g mol^{-1}) makes SIBs have a lower energy density.[8,9] Moreover, due to the difference in ionic radius of Na$^+$ (1.02 Å) and Li$^+$ (0.76 Å),[6] the diffusion properties and storage mechanisms in the host materials are considerably different in LIBs and SIBs. The commonly used graphite-based anodes in LIBs are unsuitable for direct application in SIBs.[10,11] Nevertheless, carbonaceous materials are among the most promising anodes for SIBs due to their abundance, high stability, and suitable charge/discharge voltage plateaus.[12] Significant research efforts have been devoted to achieving performance stability in SIBs. Optimizing the nanostructure and composition is required to facilitate ionic/electronic transport and buffer the volume change during cycling.[13,14] The combination of a hierarchical porous structure with heteroatom doping has been proven to be a particularly effective strategy.[15] The pore architecture influences ionic adsorption. Coupling hierarchical pore structures with the introduction of N defects in carbon layers helps to provide a high amount of active nucleation sites for sodium deposition and increases the material's capacitance through ionic diffusion enhancement.[16–18] Among different carbonaceous materials, porous hollow carbon spheres (PHCSs) perform well in LIBs and SIBs, rendering higher reversible capacities under both low and high current densities.[19,20] PHCSs are also an ideal model system for operando TEM experiments for studying specific details of electrochemical processes since they do not require additional TEM sample preparation, provide necessary electron-beam transparency, and their structure/chemical composition can be easily adapted for further optimization.[21]

J. Hou, Z. Song, M. Odziomek, N. V. Tarakina
Colloid Chemistry Department
Max Planck Institute of Colloids and Interfaces
Am Mühlenberg 1, 14476 Potsdam, Germany
E-mail: jing.hou@mpikg.mpg.de; nadja.tarakina@mpikg.mpg.de

**ADVANCED
SCIENCE NEWS**

www.advancedsciencenews.com

**NANO · MICRO
small**

www.small-journal.com

Several possible sodium storage mechanisms, such as insertion, adsorption, the combination of adsorption and insertion, and the multistage mechanism, have been proposed in the literature.[22–26] For instance, Dahn et al. suggested that sodium follows the insertion-adsorption mechanism during storage in hard carbons. The slope region is assigned to the ionic insertion between carbon layers, while the plateau region corresponds to the ionic adsorption in the micropores.[27] On the contrary, Cao et al. proposed the adsorption-insertion mechanism, where sodium ions adsorb firstly on the surface active sites and carry on with intercalation into graphene layers forming NaC_x compounds.[28] Two opposite proposals regarding the assignment of slope and plateau regions to either intercalation or adsorption processes are still under debate in the community.[23,26,29,30] Operando investigations of the dynamic behavior of sodium transportation and storage are essential to resolve the active sites for each possible storage mechanism and elucidate the intrinsic thermodynamic and kinetic processes involved in the carbonaceous sodium-ion anode. Although the fact that different in situ techniques, such as in situ X-ray diffraction, in situ atomic force microscopy, in situ X-ray absorption spectroscopy, and in situ Raman spectroscopy have been applied on cell, electrode, and material levels during the electrochemical cycling of SIBs, as well as dopants containing porous materials,[31–36] all of these techniques are missing the nanoscale spatial resolution. In comparison, in situ transmission electron microscopy (TEM) has the capability to precisely track sodium ions' migration from the interface between electrode and electrolyte and to directly observe the ion deposition into the electrodes during the electrochemical cycling. In addition, TEM-related spectroscopy techniques can characterize the structural and chemical evolution of electrode materials.[37–40] However, most in situ TEM studies use the solid-state electrolyte. Few of them have been performed on PHCSs, and their main focus has been limited to the morphology change during sodiation.[21,41] Operando investigations in commercial liquid electrolytes condition have not been performed yet. We believe such investigations are highly relevant since their conditions are closer to real devices and should provide an explicit understanding of the sodium storage mechanism by tracking the microbattery dynamics and monitoring transient states of PHCSs during sodiation in the organic electrolyte.

Herein, we set up an experiment where the nanoscale PHCSs anode is cycled within the organic electrolyte in liquid phase TEM. The size and shape of PHCSs enable direct observation of sodium adsorption or insertion at different stages of galvanostatic sodiation and at the nanoscale. Nitrogen doping has been introduced to increase the number of active nucleation sites for sodium deposition. In this work, by interpreting and associating both ex situ characterization on nitrogen-doped PHCSs (N-PHCSs) harvested from coin cell and operando tests on individual N-PHCSs in liquid phase TEM, we were capable of resolving the three-step sodium storage mechanism of the porous anode host material and highlight its charging rate dependence.

2. Results and Discussion

2.1. N-PHCSs Synthesis and Characterization

The N-PHCSs are synthesized using a hard-templating method, as illustrated schematically in **Figure 1**a. First, a nitrogen-doped resorcinol-formaldehyde (N-RF) resin shell is prepared on SiO_2 particles through the polymerization of a mixture of ethyl alcohol and aqueous ammonia, in which tetraethyl orthosilicate (TEOS) and cetyltrimethylammonium bromide (CTAB) are added as pore-forming agents.[21] Subsequent annealing is carried out under Ar atmosphere at 800 °C for 4 h. N-PHCSs are obtained by etching away the SiO_2 core using 4 M NaOH aqueous solution. A detailed description of the syntheses is given in the "Experimental section". Figure S1 (Supporting Information) shows secondary electron scanning electron microscopy (SEM) images of the particles at different synthesis stages. As-prepared N-PHCSs possess well-defined spherical morphology and uniform size. The outer diameter of the carbon spheres measured based on SEM images is 290 ± 16 nm, and the wall thickness is 25 ± 2 nm. The energy-dispersive X-ray maps collected in the scanning transmission electron microscope (STEM-EDX maps) display the homogenous distribution of nitrogen in the carbon shell (Figure 1b). Both EDX spectra (Figure S2, Supporting Information) and Fourier transform infrared (FTIR) spectra (Figure 1c) confirm the completion of the core etching. The characteristic adsorption peaks of Si–O–Si and O–Si–O at 1030 and 789 cm^{-1}, respectively, disappeared from FTIR spectra after etching.[42] The broad peak at 1000–1600 cm^{-1} corresponds to the sp^2 carbon-conjugation. The N_2 sorption at 77 K was exploited to characterize the nanoporosity; the isotherms are shown in Figure S3 (Supporting Information). The specific surface area of 290 $m^2 g^{-1}$ was determined by the Brunauer–Emmett–Teller (BET) method. The pore size distribution and cumulative pore volume, shown in Figure 1d, were calculated from the adsorption branch of the isotherm (Figure S3, Supporting Information) using quenched solid density functional theory (QSDFT) kernels. N-PHCSs samples possess 35 vol% micropores (<2 nm) and 65 vol% small mesopores (2–4 nm).

2.2. Stepwise Microscopy Analysis of Sodium Storage in N-PHCSs from Coin Cell

In order to clarify the sodium storage behavior of N-PHCSs, half-cell cycling is firstly measured at C/15 between −0.07 V to 2 V versus Na/Na^+ in coin cells. The electrolyte consists of 1 M $NaPF_6$ in 50 vol% ethylene carbonate (EC) and 50 vol% diethyl carbonate (DEC) with 5 wt% fluoroethylene carbonate (FEC). Stepwise SEM characterization on the harvest electrodes at three distinct voltage regions was observed in the characteristic charge−discharge potential profiles (vs Na/Na^+): a steep sloping region before 1.3 V, a second slope above 0.1 V, and a plateau at −0.05 V (**Figure 2**a).

The corresponding SEM image of the sodiated electrode after the slope region shows N-PHCSs loosely in contact with each other displaying just subtle morphology changes (Figure 2a). According to EDX data, sodium content in N-PHCSs increases up to 14 at.%. The slope change from ≈1.3 V suggests different capacity contributions in these two slope regions: capacitive contribution from ionic adsorption on energy preferential sites with heteroatom substitution at potentials >1.3 V followed by charge transfer reactions at potentials <1.3 V. Shell thickness expands, and the gaps between spheres are filled after the plateau region beneath 0.1 V. Hollow carbon spheres are covered entirely by a solid phase, which binds them to a continuous medium.
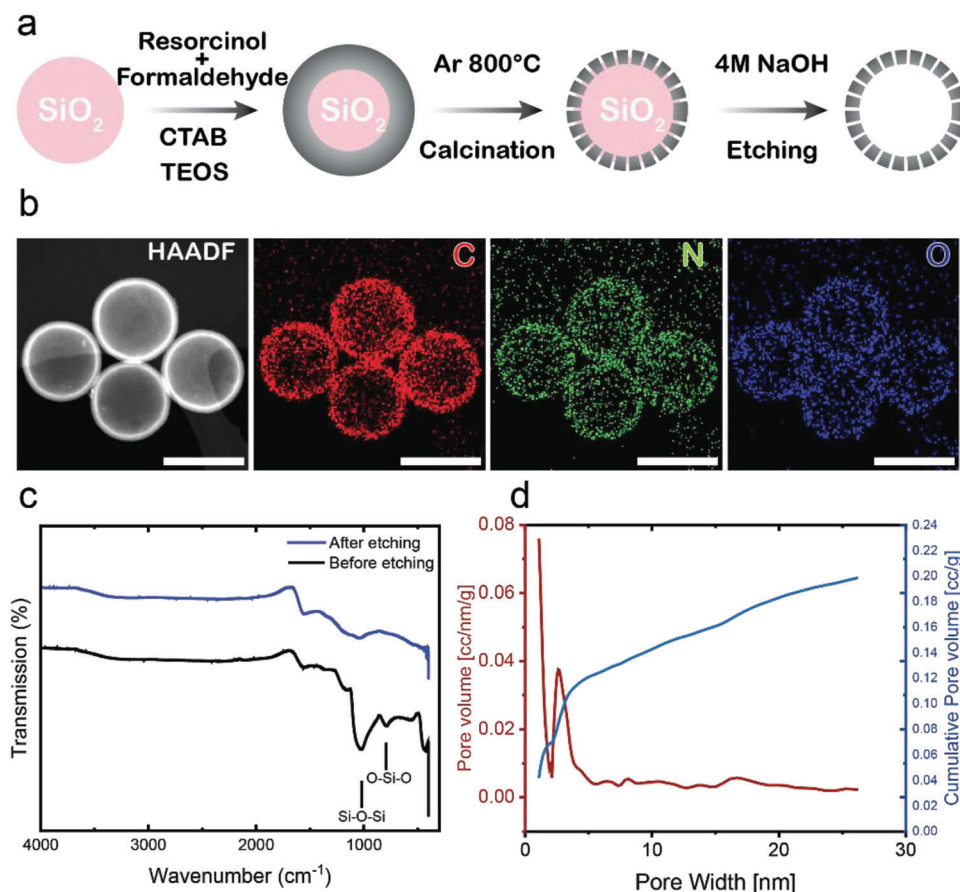
Figure 1. a) Schematic of the hard-template synthesis of N-PHCSs; b) ADF-STEM image of the N-PHCSs and corresponding EDX maps, representing signals of C, N, O; c) FTIR spectra of N-PHCSs before (black) and after (blue) etching with NaOH. d) The pore size distribution (red) and cumulative pore volume (blue) in N-PHCSs were obtained based on nitrogen adsorption data at 77K.

These electrode morphology changes occur with sodium content increasing to 20 at.% (Figure 2a). After stripping, the sodium content drops down to 7 at.%, leaving only patchy patterns on the surface of the N-PHCSs, while most bulky phases between spheres have been withdrawn. As the sodium content is unchanged ($\approx$6 at.%) after subsequent discharge to 1.3 V (Figure S4, Supporting Information), we assume that the capacity contribution should be mainly assigned to the absorption of Na$^+$ on the surface of carbon nanospheres in the first sloping region.

Additionally, the morphology comparison of pristine (Figure 2b) and cycled (Figure 2c) N-PHCSs with TEM explicitly revealed an increase of the outer sphere diameter by $\approx$19 nm while the hollow space shrunk by $\approx$18 nm in diameter based on the statistic size measurements on a larger sample volume from images at lower magnification (Figure S5, Supporting Information). On average, the sodiated carbon shell has expanded from 25 to 44 nm. The direct visualization over dimension changes suggests sodium deposition on both sides of the carbon shell and storage inside the porous shell. Furthermore, the distinguishable contrast change in the ADF-STEM images in Figure 2c and the concentrated sodium and oxygen signals within the ring-shaped carbon shell in the elemental EDX maps after cycling in Figure 2d support the hollow-core-filling hypothesis. However, quantitative analysis of sodium

deposition outside and inside the porous shell as well as on the current collector from galvanostatic charge/discharge curves is challenging because of these phenomena simultaneous contributions once the energy barriers of heterogeneous nucleation is overcome. The presence of oxygen is a result of sodium oxidation during the unavoidable exposure to air during the ex situ sample preparation (as described in the Experimental Section).

According to the previous study by Cao et al., the first steep slope should correspond to the ionic adsorption to active sites at the surface of the hollow structure.[28] The voltage-dropping rate decrease is caused by the primary NaF formation due to the decomposition of FEC at $\approx$1.3 V.[43–45] The second sloping region can most probably be correlated with the sodium ions diffusion inside the carbon shell, ionic absorption at the binding sites and edges of the carbon matrix.[18,23,46,47] The presence of nitrogen defects with high adsorption enthalpy enhances sodium sorption, and the considerable amount of micropores in the carbonaceous material increases ionic conductivity by increasing the specific surface of materials.[16–18,21,48] Combining these two factors enables forming more active nucleation sites for sodium deposition on the carbon surface in elemental states or clusters. The plateau region under 0.1 V is typical for sodium deposition in the non-graphitized and microporous shell of the carbon spheres.[30,49] As a result of the Na$^+$/e$^-$ pairs saturation at
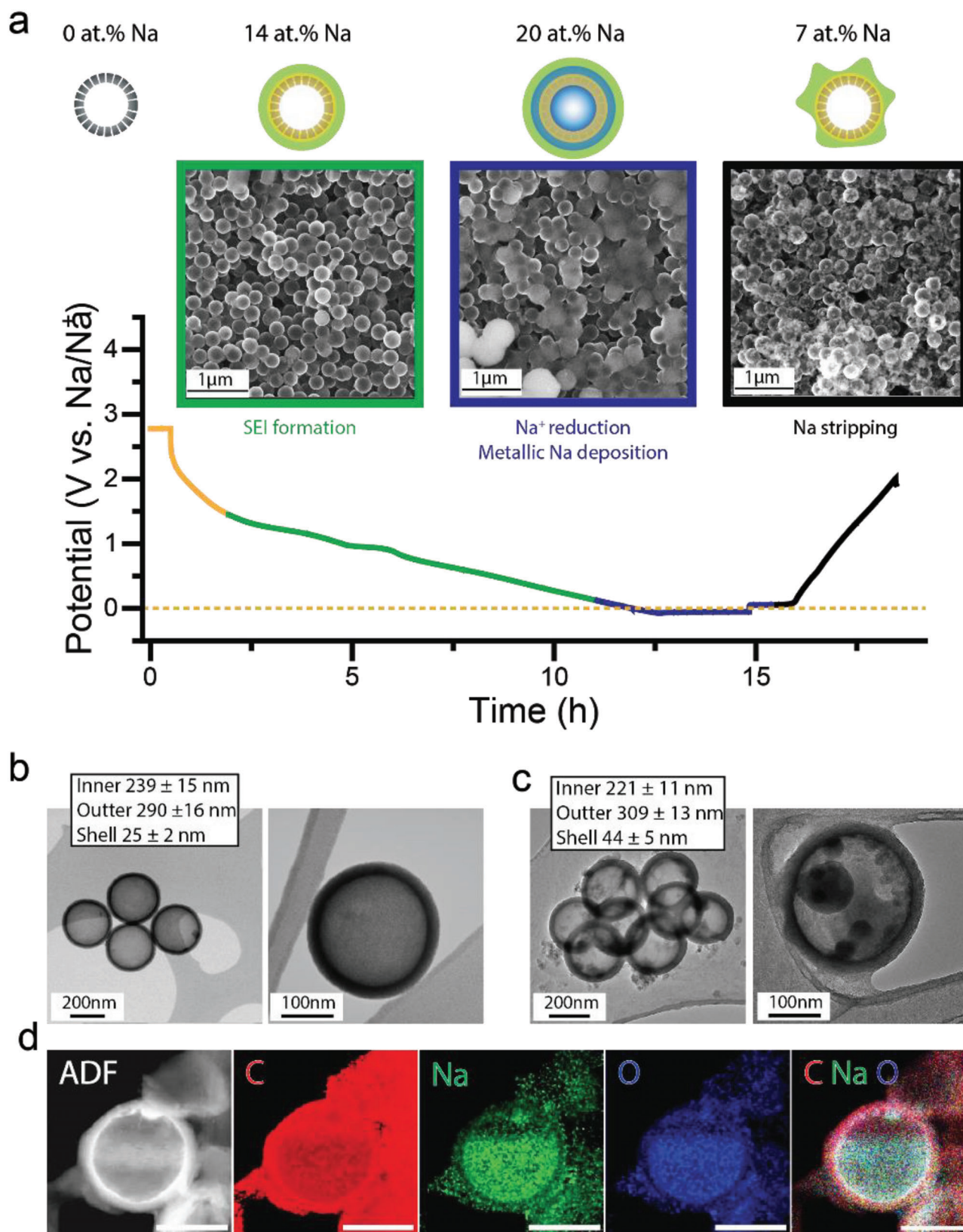
Figure 2. Stepwise ex situ analysis of sodium storage in a coin cell. a) SEM images of N-PHCSs at different stages of sodiation and schematic illustration of the sodiation procedure with Na content detected by EDX. The adsorbed sodium ions are shown in yellow. SEI is demonstrated in green. Deposited Na is indicated in blue. TEM images of b) pristine and c) sodiated N-PHCSs . d) EDX maps of sodiated N-PHCSs. The scale bar corresponds to 200 nm.

**ADVANCED
SCIENCE NEWS**

www.advancedsciencenews.com

**NANO · MICRO
small**

www.small-journal.com

the electrode–electrolyte interface, the reduction of Na^+ to $Na(0)$ happens before reaching the nucleation potential; it is usually described as underpotential deposition.[50] Such deposition becomes more energy favorable in the nanostructured materials with micropores due to the low cohesion energy of $Na(0)$ with C.[18] Accumulation of quasi-metallic sodium in defective carbon micropores under such nonequilibrium conditions has been observed using small-angle X-ray scattering (SAXS), wide-angle X-ray scattering (WAXS), and in situ nuclear magnetic resonance (NMR).[51,52]

Unlike the deposit sodium that can strip away during desodiation, SEI formation is irreversible, leaving patchy traces on the surface of spheres, binding N-PHCSs by sealing the empty space in between (Figure 2a). This brings new insights into the function of the electrode with spherical particles. By assembling into a continuous phase by SEI during cycling, the N-PHCSs electrode performs as a protective layer for sodium ion penetration and deposition on the current collector, leading to significant capacity improvement from controlled electroplating. Furthermore, it is coherent with the compact solid layer of sodium metal observed under the electrode layer (Figure S6, Supporting Information), which is considered the main contribution to the capacitance after crossing the nucleation potential. Unfortunately, this patchy decoration on the surface of N-PHCSs after cycling is not visible in ex situ TEM analysis because the organic components in SEI, such as NaF and Na_2CO_3, cannot be fully preserved after the sample preparation with sonication in ethanol.[53] Therefore, a non-destructive, real-time analysis technique is required for studying the dynamics of the sodium storage and the evolution of SEI formation of the electrode within batteries.

2.3. In Situ TEM Analysis of Sodium Storage in N-PHCSs from Liquid Cell
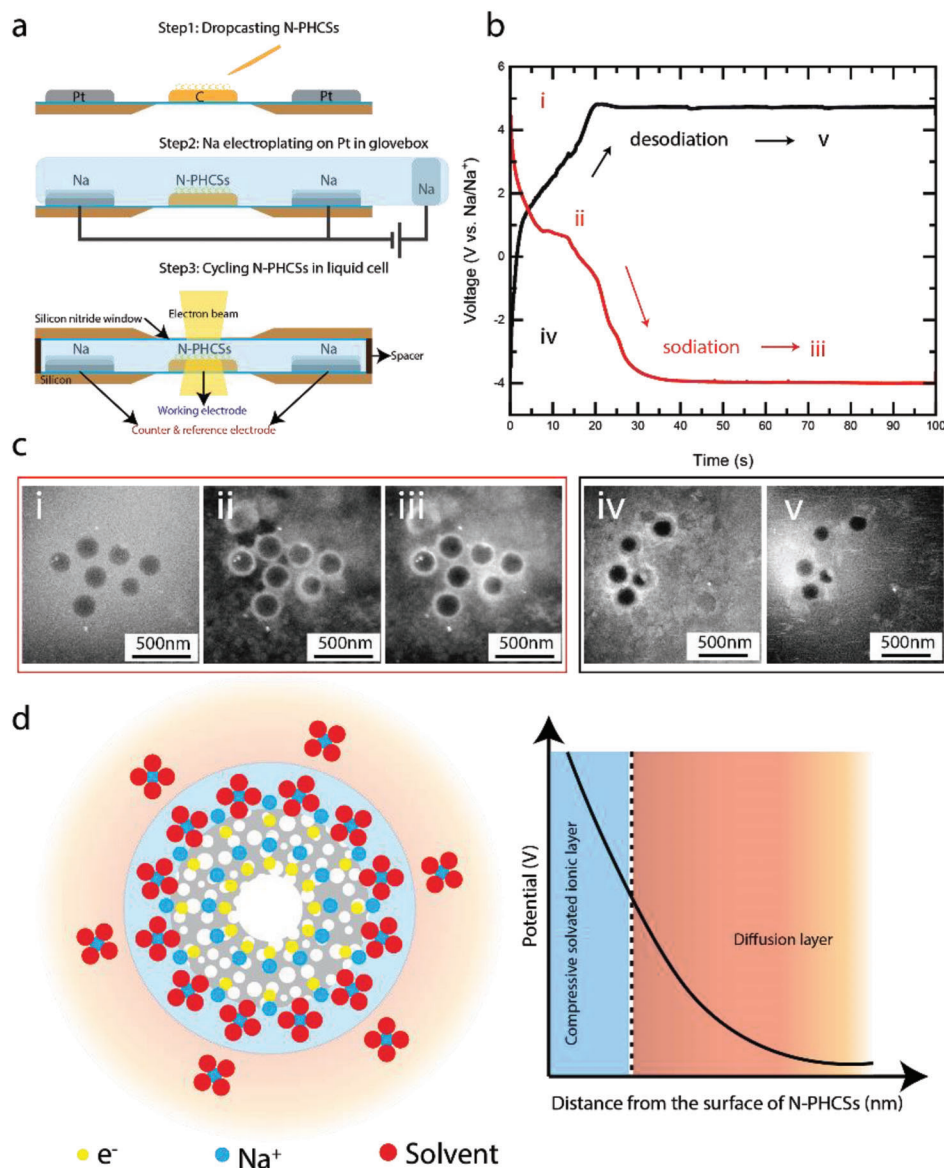
2.3.1. Microbattery Assembly in the Liquid Cell

The microbattery with N-PHCSs as a working electrode and electroplated sodium as a counter and a reference electrode is assembled in a sealed liquid cell, as illustrated in **Figure 3**a. The suspension of N-PHCSs in N-Methyl-2-pyrrolidone (NMP) is dropcasted on the glassy carbon electrode patterned on a commercially available electrochemical chip. Then the chip is mounted on a homemade glass cell to electroplate sodium on the platinum electrode; the latter is used as the working electrode, while a piece of metallic sodium is connected as the counter and reference electrode. Electroplating is assumed to be completed when a stable potential reading reaches 0.1 V between the electroplated platinum electrode and the metallic sodium. The thickness of the deposited Na layer is kept below 60 nm, which is controlled by applying −5 μA currents for 300 s. The morphological and compositional changes of the electrode after electroplating are confirmed using SEM-EDX (Figure S7, Supporting Information). Once the two electrode materials are precisely loaded on the electrochemical chip, as illustrated in the first two steps in Figure 3a, the liquid cell is assembled by enclosing the liquid electrolyte between two silicon chips with their electron-transparent membranes aligned. The spacer-defined liquid layer thickness is 500 nm. Both the electroplating of sodium and the assembly of the liquid cell are carried out in an argon-filled glovebox to avoid sodium oxidation and electrolyte degradation.

2.3.2. Microbattery Cycling in the Liquid Cell

The specific capacity of the working electrode in a liquid cell system cannot be estimated since the mass loading achieved during drop-casting of N-PHCSs is hard to control. The Ohmic drop in thin liquid layers was shown to be so significant that the potential range for running a complete cycle over electrode materials cannot be directly transferred from the macroscale setup.[54] Therefore, in order to demonstrate that in situ electrochemistry reproduces well-established criteria even within the system limitations, the in situ liquid cell experiments were conducted at an adapted current scale, achieving the characteristic voltammetry profile of N-PHCSs cycling, regardless of the electron beam. The galvanostatic charge/discharge profile in Figure 3b demonstrated an inherent compromise between spatial resolution imaging and semi-quantitative electrochemistry. The setup replicates the results of a conventional electrochemical cell by running charge/discharge cycles at a constant current of 2 nA in the microbattery setup. The curves are reproducible with and without the electron beam.

One can see from Figure 3c-i that N-PHCSs are immersed in the electrolyte as no sharp edge of the carbon shells is visible. Soon after the sodiation starts, within the first 10 s, the distinct change in the contrast between the electrolyte background and the N-PHCSs is observed, indicating the formation of the solvated ionic layer on the surface of the N-PHCSs due to the strong electron binding with sodium ions (Figure 3c-ii). One has to note that the described change turns less notable during the subsequent sodiation process due to the formation of the SEI, which has a much stronger mass-thickness contrast on the image. The pronounced concentration gradient of sodium ions across the relatively thin mass-transfer boundary layer (<40 nm) leads to a current density-dependent concentration polarization.[55] The deviation from the reversible potential for N-PHCSs anode cycling in the coin cell test and the measured potential during the operando TEM experiment is coherent with the instantaneous concentration polarization from the solvated ionic layer formation. Consequently, the measured potential under the high current density is a combined result of electrolyte ohmic resistance and the concentration overpotential. Although the specific area current density in the liquid cell (0.1 mAh cm^{-2}) is only four times higher than that in the coin cell (0.025 mAh cm^{-2}), the mass loading per unit area of the coin cell can be roughly estimated as 100 times higher than for the liquid cell. Thus, the N-PHCSs cycled in the liquid cell are under accelerated cycling conditions. The corresponding significant electric field gradient eventually drove the system into a nonequilibrium condition, leading to intense electrode polarization. Nevertheless, sodium ion diffusion and reduction are preferable due to both the N-doping and the curvature of spherical particles within the hollow sphere.[56,57] Sodium storage occurs mainly through the reduction reaction on the outer surface of the spheres under the plateau potential, where a continuous solid phase has formed and linked the N-PHCSs together, as shown in Figure 3c-iii.

**ADVANCED
SCIENCE NEWS**

www.advancedsciencenews.com

NANO · MICRO

small

www.small-journal.com

Figure 3. a) Schematic of liquid cell preparation and assembly for in situ TEM analysis on N-PHCSs. b) The curve of N-PHCSs sodiation and desodiation in TEM at a constant current of 2 nA for 100 s and corresponding STEM images. c) STEM images (i–v) from different states of charge are indicated in the plot. Images in the red rectangle are taken during sodiation, while the ones in the black rectangle are from desodiation. d) Schematic illustration of compressive solvated ionic layer formation on the surface of N-PHCSs (left) and the potential distribution from the surface of the sphere to the electrolyte as a function of the distance (right).

The desodiation procedure is followed on another viewing region in order to exclude the effect of previous electron beam irradiation. As shown in Figure 3c-iv, similar to the first field of view, particles after sodiation display a thickening of their shells (40–60 nm). Solid phases consist of high-contrast compounds on the surface of sodiated N-PHCSs and the glassy carbon substrate to which particles are loaded. During desodiation, the circle-shaped deposition and the substrate decoration strip away without much change in the thickness of the shell (Figure 3c-v).

From the operando observation, we were able to clarify that at the initial step of sodiation, the formation of a solvated ionic layer on the surface of N-PHCSs occurs, which is followed by the irreversible shell expansion due to the SEI formation and subsequent

storage of Na(0) within the porous carbon shell (the slope region). Instead of the previously reported interlayer insertion and ionic adsorption theory proposed by Dahn et al. and Cao et al., both diffusion of sodium ions into the preferential sites and reduction of sodium on the surface and within pores of carbon shells have been affirmed to take place during the slope region in the sodiation profile. This phenomenon is coherent with the observation from ex situ analysis on particles cycled in the coin cell. Additionally, according to the operando observation and stepwise SEM tracking of the sodium storage path, the plateau region coincides with the preferential sodium deposition on the inner surface of the carbon shells rather than the previously reported meso/micropore filling.[22] Nevertheless, the porous structure of

**ADVANCED
SCIENCE NEWS**
www.advancedsciencenews.com

NANO · MICRO
small
www.small-journal.com
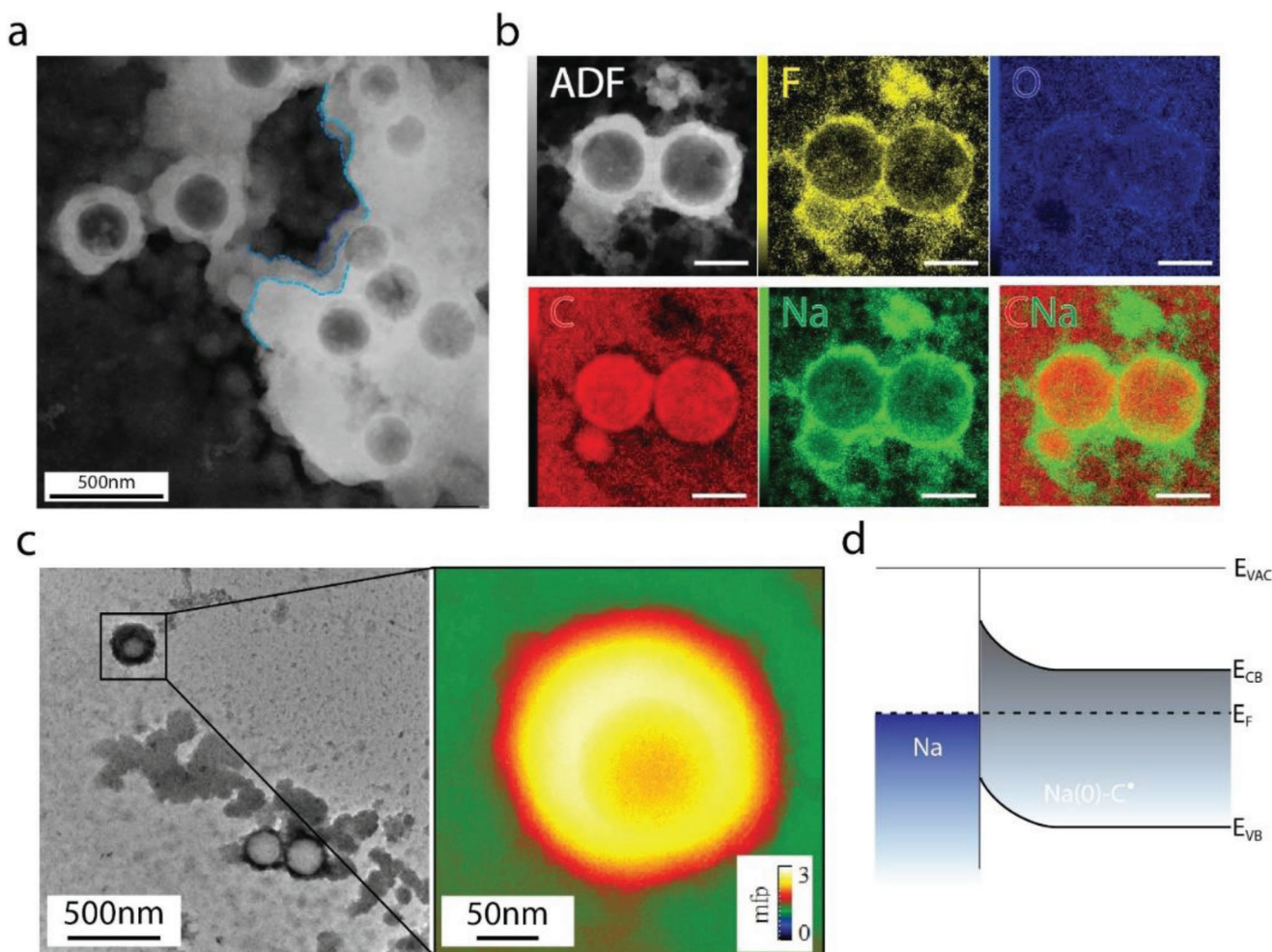
Figure 4. a) STEM images of sodiated N-PHCSs. Blue lines indicate the layer boundary of deposition sodium layers under shells. b) STEM image and EDX mapping of sodiated N-PHCSs; the scale bar corresponds to 200 nm. c) TEM image (greyscale) of sodiated N-PHCSs and thickness mapping (color) over one carbon sphere indicated on the TEM image. d) Schematic illustration of band edge drift at the interface of a metal-semiconductor junction.

the carbon shell influences charge carrier transport significantly. Mesopores guarantee the solvated ions diffusion in the organic electrolyte at low current density conditions, where solvated ions have been reported to be larger than 1 nm.[58] Micropores enhance ionic transport by increasing the surface area and hosting quasi-metallic Na during sodiation, which consequently modifies the local electronic structure of carbon. We presume this local electronic structure modification shall be the reason for the preferential deposition within the hollow structure, as can be inferred from a preliminary analysis of cycled N-PHCSs (Figure S8, Supporting Information). Ex situ electron energy loss spectroscopy (EELS) analysis of the cycled N-PHCSs from the liquid cell will be discussed below to resolve the reason for this preferential deposition.

2.3.3. Analysis of Cycled N-PHCSs from Liquid Cell

In order to overcome the resolution limitation within the liquid phase TEM, post-mortem analysis on the sodiated N-PHCSs is conducted. The liquid cell is disassembled within an argon-filled glovebox and rinsed with DEC to remove the NaPF$_6$-containing electrolyte, from which the SEI layer can be properly preserved. The chip is then stored in the glovebox to minimize the air exposure time. A home-designed ex situ holder is applied for examining the chip. **Figure 4**a–c shows the STEM images of some representative N-PHCSs after cycling in the liquid cell. Most of the particles appear hollow inside but are connected by a continuous solid phase that is rich in Na and F, as characterized by EDX (Figure 4b). The FFT obtained from a high-resolution TEM image of this binding phase points to the possible existence of NaF (*Fm3m*) nanocrystals distributed in the dominant amorphous matrix (Figure S9, Supporting Information).[59] The carbon shell and the interface between N-PHCSs and the electrolyte can be easily differentiated since carbon and fluorine signals in the EDX maps have distinct boundaries. Therefore, we assign the critical phase around particles to the SEI layer. This SEI layer formed on the surface of N-PHCSs is rather irregular in thickness and considerably changes the morphology of the particle due to the inhomogeneous electric field-dependent SEI

**ADVANCED
SCIENCE NEWS**
www.advancedsciencenews.com

NANO · MICRO
small
www.small-journal.com
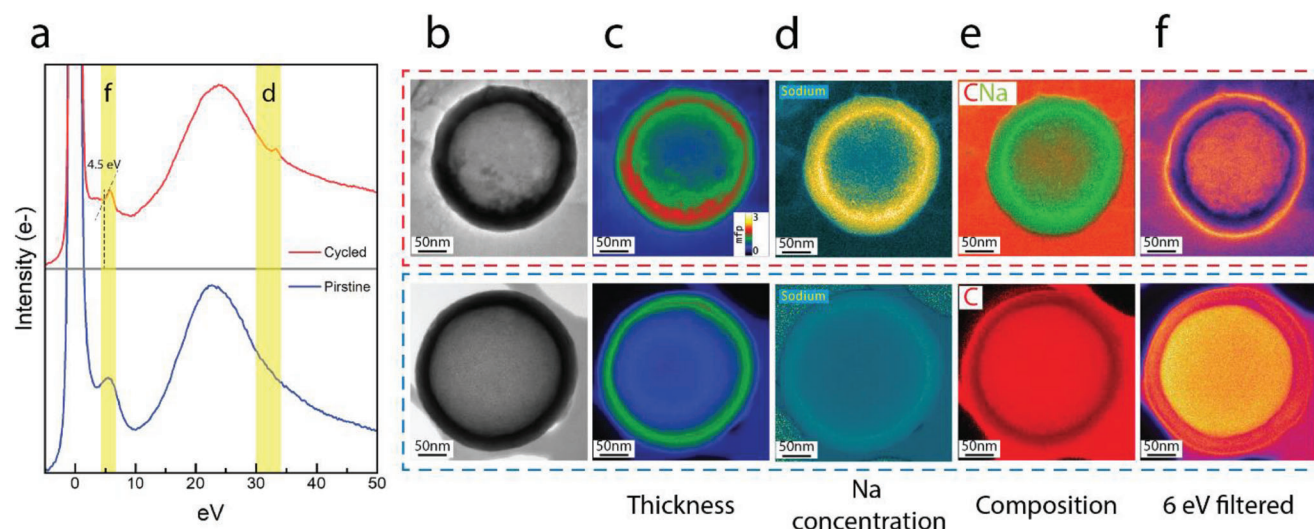
Figure 5. Comparison of EFTEM on pristine and cycled N-PHCSs. a) Low-loss EELS comparison of pristine and cycled particles. b) TEM images and c–f) EFTEM images; comparison of pristine (in the blue dashed rectangle) and cycled particles (in the red dashed rectangle). c) Thickness mapping corresponds to the EFTEM of the ZLP with a 12 eV slit. d) Na K edge mapping from 28 to 32 eV. e) Composition mapping combines C K edge mapping from 272 to 294 eV and (d). f) Electron density and sodium mapping correspond to the selected energy range between 4−6 eV and 30−34 eV, respectively, as highlighted in yellow in (a).

formation on the surface. The SEI enhances the contact surface between particles, facilitating charge transfer. Apart from the transfer from the electrolyte to the N-PHCSs surface, the sodium ions transport through the SEI-filled gaps between spheres results in the sodium deposition between the electrode layer and the current collector, respectively, as observed previously in Figure 4c. The solid-phase layers below N-PHCSs are the deposits of Na which can be associated with the Na deposited underneath the electrode layer in the coin cell test.

In addition, a few particles have shown excessive sodium content within the voids of hollow spheres, presenting a dark contrast within N-PHCSs on the TEM image, Figure 4c. Although not dominant, the thickness map obtained from one of such spheres using EFTEM (Figure 4c) shows a thicker ring inside the shell, suggesting that the Na-filling is growing radiantly from the inner surface of the carbon. This growth trajectory indicates the preferential deposition at the interface between sodium and carbon inside the hollow sphere, contrary to the typical sodium deposition through nucleation and growth. This unusual preferential deposition at the interface can be explained by the formation of the Schottky barrier between deposited sodium on the inner surface and semiconductive carbon, at which the energy barrier is smaller for electrons moving towards sodium from the carbon shell.[60,61] Since the electronic structure of carbon can be tuned by dopants, defects, and nanofillers, as has been reported by Li & Antonietti,[62] the N-doped carbon with micropores filled with Na(0), in our case, performs as a semiconductor-like material. Wang et al. have also reported a quasi-solid state reaction inside the confinement of Na-filled micropores.[63] The quasi-metallic Na, in this case, forms a bond with the surrounding carbon, the degree of the ionic character of this bond can be estimated using the Haney-Smith equation (Equation S1, Supporting Information). The significant electronegativity difference between sodium (0.93) and carbon (2.55) makes the bonding

highly polar.[64] More electronegative carbon attracts electrons from less electronegative sodium, consequently leading to local electron-rich conditions within micropores. Experimentally, this phenomenon can be confirmed from EELS analysis of sodiated carbon where the decreased sharpness of the π^* peak of C K-edge reflects a contribution from carbon disorder after Na incorporation (Figure S8, Supporting Information) and from analysis of valence region of EELs spectra (**Figure 5**d). As illustrated in Figure 4d, E_{VAC}, E_{CB}, and E_{VB} indicate the energy level of the vacuum, the conduction band, and the valence band of the semiconductor, respectively; E_F corresponds to the drifted Fermi level at the interface. We hypothesize that the metal-semiconductor junction is formed by the contact between the deposited sodium layer on the inner surface of N-PHCSs and the N-doped carbon shell, where the band edge drift increases the electron density in the metal at the interface. To support the proposed mechanism, we performed detailed EFTEM experiments, which will be described in detail in Section 3.2.

In contrast to the ex situ experiment, in situ cycling in the liquid cell leads to sodium being mainly stored within the carbon shell rather than filling the hollow space of the spheres. This happens due to the kinetic limitation from ionic diffusion under the accelerated cycling condition in the liquid cell. The limited mass loading of N-PHCSs in the liquid cell makes the applied current density for the microbattery cycling a few hundred times higher than the current density normally applied in the coin cell system. Such high-rate cycling conditions emphasize the capacitive contribution as a more significant concentration gradient is formed, leading to a broader diffusion layer with solvated ions in the electrolyte. Such correlation with the kinetics of battery cycling has also been reported by David et al.[23,24,65,66] The current density could reach such a level that concentrated adsorbed sodium ions driven by the current at the initial stage do not have sufficient time to transport through the carbon shell. Consequently, more

rapidly sodiated N-PHCSs tend to have less sodium filling inside. This hypothesis is supported by the absence of hollow-filling sodium within N-PHCSs through cycling in the coin cell under high current density (0.04 mA cm^{-2}) (Figure S10, Supporting Information). In contrast, the above-described observation from a coin cell experiment performed at a relatively low current density (0.025 mA cm^{-2}) shows considerable filling inside the voids of N-PHCSs. Even though the microcell setup offers us a chance to monitor the sodiation procedure in the liquid phase TEM, the limitation of electrochemical cycling conditions hinders the insertion of sodium into the hollow sphere. That is why analytical microscopy studies were performed on the particles harvested from the coin cell test to understand the storage mechanism of the void filling in N-PHCSs.

2.3.4. EFTEM Analysis on the Sodium Storage Mechanism in N-PHCSs

During sodiation, sodium ions can penetrate into the micropores in the carbon shell, hypothetically changing the electronic band structure and leading to preferential deposition at the metal–carbon interface. Valence EELS (VEELS) is an ideal tool to monitor changes in the electronic structure of the materials at the nanoscale and to track the lithiation states of electrodes.[67] Here we employed VEELS to study the sodiation states of our N-PHCSs-based anode. Energy-filtered TEM (EFTEM) images and the corresponding EEL spectra of pristine and cycled N-PHCSs are shown in Figure 5a. The broad bump at 5.4 eV observed from the pristine sample corresponds to a characteristic intraband transition from π to $\pi*$ for carbonaceous materials.[68,69] After sodiation, two additional distinct features appear on the EEL spectra: 1) a fingerprint at 5.7 eV in the low-loss region and 2) a peak at 32 eV. The first peak corresponds to a bulk plasmon of Na(0),[70] while the second peak is the Na $L_{2,3}$ edge.[71] The latter does not show many fine-structure details apart from sharpening at the edge, suggesting that Na is present mainly in the metallic form. The distinct bandgap opening at 4.5 eV indicates a change in electronic structure due to induced local strain from Na(0) in the micropores.[72] The contact between the metallic sodium layer deposited on the inner surface of N-PHCSs and the semiconductor-like carbon shell forms the metal-semiconductor junction in the N-PHCSs.[60,62]

The EFTEM analysis of freestanding N-PHCSs was conducted over a selective energy range before and after sodiation (Figure 5c–f) to resolve the spatial distribution of these featured signals. The thickness maps are taken with a 12 eV slit over the zero-loss peak (ZLP). The contrast on the thickness map for the cycled N-PHCSs is consistent with one observed on the TEM images (Figure 5b,c). Furthermore, the significant intensity increase on the inner surface of the carbon shell observed on the cycled N-PHCSs thickness map (Figure 5c) is in agreement with the Na signal distribution in Figure 5d, suggesting that sodium accumulates between the carbon shell and initially deposited sodium inside N-PHCSs. EFTEM maps of carbon and sodium signals in Figure 5e also prove that the sodium is stored within the carbon shell in the form of SEI or clusters and is also deposited on the inner surface of the shell inside the hollow space of N-PHCSs. The potential electronic structure transformation of carbon shells af-

ter sodiation can be supported by the contrast gradient change after sodiation on the carbon shell from the EFTEM maps taken in the energy range between 4−6 eV, Figure 5f. More specifically, the broader and sharper signal intensity gradually drops from the outer surface of cycled N-PHCSs toward the inner surface of carbon shells, suggesting the redistribution of the electron density at the Schottky junction. While in the case of uncycled N-PHCSs, despite a thin bright line at the edge of the sphere, no sharp intensity changes are observed within the hollow space and over the carbon shell.

Summarizing the above experimental results, we can say that this work explicates sodium storage mechanisms in N-PHCSs in carbonate-based electrolytes at the nanometer scale by combining the ex situ study and the direct visualization of the sodiation process using operando liquid phase TEM. As illustrated in **Figure 6**a, N- doping and the pore architecture of N-PHCSs enhance sodium diffusion into the carbon shell and a preferential Na$^+$ reduction within the micropores. The formation of Na(0)-C polar covalent bond changes the electronic structure of N-doped carbon; a Schottky junction forms at the interface between the inner surface of N-PHCSs and a Na layer deposited on this inner surface. The reduced energy barrier of this Schottky junction results in uniform Na deposition at the inner interface. The whole sodiation procedure is accompanied by Na and F-rich SEI formation (Figure 6a). Because of the relatively loose stacking of N-PHCSs, sodium ions can easily penetrate through the layer of carbon spheres and reach the surface of the current collector. SEI fills the gaps between nanospheres within the N-PHCS-based electrode, subsequently facilitating the transport of solvated sodium ions toward the surface of N-PHCSs and between them until reaching the current collector. The sodium plating then takes place at overpotential conditions. Thus, as illustrated in Figure 6, the self-stabilized binding between spheres by SEI makes the N-PHCSs electrode behave like a protective layer between the current collector and electrolyte, suppressing dendrite formation on top of the anode.

Depending on the current density, sodium ions are stored at different regions of N-PHCSs (Figure 6b). Sodium ions transport through the interconnected micro/mesopores on the carbon shell and accumulate both in the pores of the carbon shell and voids of hollow spheres at low current densities without experiencing a severe ionic diffusion limitation. The kinetic limitation of ionic diffusion becomes more significant at higher current density conditions, favoring the accumulation of the sodium ions inside the carbon shell and on the outer surface of N-PHCSs other than filling the voids of N-PHCSs. Although Na deposition can happen inside the spheres at a low current density, most of the contribution to the capacity still comes from the Na plating underneath the electrode layer. This Na plating serves as an additional energy storage path beside the sodium insertion into carbonaceous materials. After desodiation, the remaining SEI patches modify the morphology of particles but still keep spheres linked with each other, preserving the transportation of sodium ions towards plating on current collectors in the following cycles.

3. Conclusion

In this work, by combining in situ TEM with ex situ SEM/TEM analysis, we were able to follow the electrochemically induced
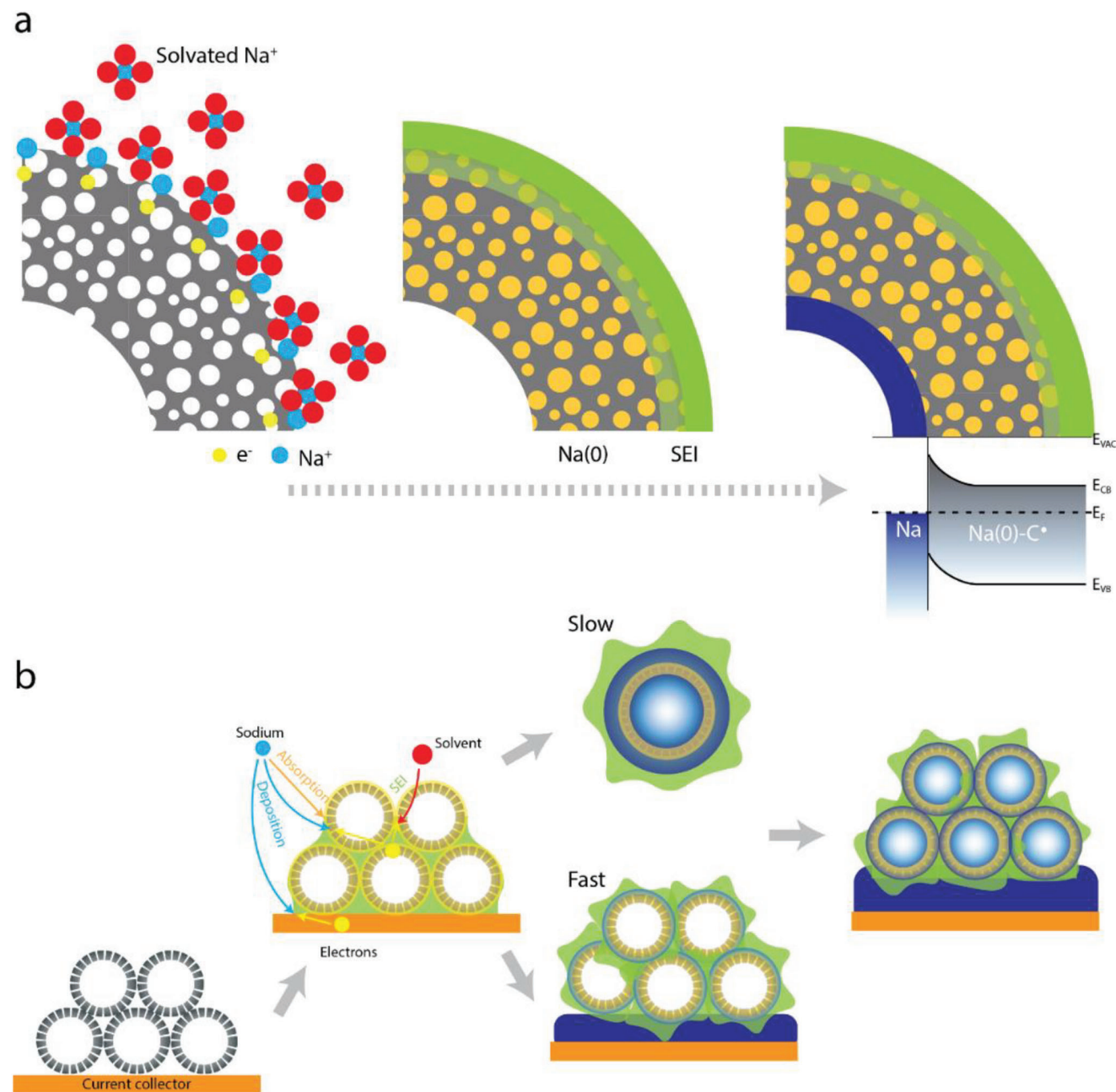
Figure 6. Schematic of sodium storage mechanism in N-PHCSs a) at the electrode and electrolyte interface and b) at the assembled electrode scale. Reduced Na(0) in micropores is shown in orange. SEI is presented in green. The deposited sodium is shown in dark blue.

evolution of the N-PHCS-based anode at the nanoscale and to propose the Na storage mechanism for such systems. We observed that the enhancement of ionic diffusion due to the nanoscale structure of spheres results in SEI formation not only on the surfaces of particles but also partially inside carbon shells. The Schottky junction formed on the inner surface of N-PHCSs facilitates the sodium deposition at the interface rather than following the path of nucleation and growth. Kinetic limitations during N-PHCSs sodiation have also been examined by monitoring the current-density-dependent sodium storage in coin cell tests and in liquid-phase-TEM microcell experiments. In addition, di-

rect visualization of the formation of the ionic layer by operando TEM and the modification of the local electronic structure of carbonaceous material at the nanoscale by EELS provide fundamental insight into the sodium storage mechanism in the N-PHCSs anode. The in situ characterization setup used in this study can be applied to examine other electrode materials and contribute to developing novel energy storage devices. Although the synergy between the liquid-cell experiments and the ex situ time-dependent characterization of the coin cell systems is a powerful combination to understand the mechanism of the electrochemical processes, further improvements in the in situ TEM experiment

**ADVANCED
SCIENCE NEWS**

www.advancedsciencenews.com

**NANO · MICRO
small**

www.small-journal.com

design and data collection are needed in order to be able to replicate the sodiation/desodiation process in conditions even closer to the actual batteries. In particular, the time resolution of the in situ measurements needs to be optimized so that the correlation between material changes and the electrochemical performance of electrodes in SIB or other energy storage devices can be thoroughly investigated at the nanoscale in dynamics.

4. Experimental Section

Chemicals: Tetraethylorthosilicate (TEOS), ethanol, ammonia solution (28 wt%), resorcinol, formaldehyde, EDA, and Diethyl carbonate (DEC) were purchased from Sigma–Aldrich. All chemicals were of analytical grade and deionized (DI) water was used for all experiments. The electrolyte of 1 M $NaPF_6$ in ethylene carbonate (EC) and DEC (1: 1, by Vol.) with 5 wt% fluoroethylene carbonate (FEC) was purchased from E-Lyte Innovations GmbH.

Synthesis of Nitrogen-Doped Porous Hollow Carbon Spheres (N-PHCSs): TEOS (6 mL) was added to a mixture solution containing 75 mL of ethanol, 10 mL of DI water, and 3.15 mL of ammonia and then stirred at 30 °C for 6 h. The SiO_2 nanospheres were centrifugally separated from the product suspension and washed with DI water and ethanol. SiO_2 nanospheres (0.5 g) were dispersed in a mixture solution of ethanol (30 mL) and DI water (70 mL). The resorcinol (0.32 g), formaldehyde (0.48 mL), and EDA (0.32 mL) were then added. After stirring for 5 min, 0.2 mL of TEOS was added as a pore-forming agent. The reaction proceeded under stirring at 30 °C for 24 h. The intermediate N-RF colloid with SiO_2 core was collected by centrifugation and then annealed under an Ar atmosphere at 800 °C for 4 h. Finally, N-PHCSs were obtained after the etching of the SiO_2 core using the 4 M NaOH aqueous solution for 12 h, and repeated for five times.

Electrochemical Measurement: All the charge/discharge profiles of batteries were measured by using Swagelok cells. N-PHCSs and the binder (polyvinylidene fluoride (PVDF)) were mixed by a mass ratio of 90:10 and dispersed in N-methyl-2-pyrrolidone (NMP). Then the obtained slurry was blade-coated on copper foils, and the coated electrodes were dried in a vacuum oven at 60 °C overnight. The mass loading of N-PHCSs on each electrode was ≈0.6 mg cm^{-2}. The galvanostatic charge/discharge tests were performed on the Biologic MPG-2 Battery Testing System. The electrolyte was 1 M $NaPF_6$ in EC/DEC (1:1, v/v) with 5 wt% of FEC. All the cells were assembled by using metallic sodium as both counter and reference electrodes in an Ar-filled glovebox. The batteries were cycled with a constant capacity of 150 mAh g^{-1} for sodiation and with a cut-off potential of 2.0 V (vs Na/Na$^+$) for de-sodiation. The samples for stepwise ex situ analysis were selected by sodiating/de-sodiating the electrodes at different states of charge.

Ex Situ Characterization: SEM images were taken using a Gemini 1550 (Zeiss AG) scanning electron microscope at an acceleration voltage of 10 kV. For the ex situ TEM characterization, cycled N-PHCSs particles were harvested from the coin cell test by sonicating in ethanol after rinsing by DEC. For post-mortem analysis, the electrochemical chip loaded with cycled N-PHCSs was mounted and preserved within an Ar-filled glovebox after removing the remaining electrolyte with DEC and before transferring it for TEM analysis. Elemental mapping and DF-STEM images were collected by a JEM-F200 Multi-purpose electron microscope with a high-angle silicon drift Energy Dispersive X-ray (EDX) detector (solid angle up to 0.98 steradians with a detection area of 100 mm^2). HRTEM, EELS, and EFTEM analysis were conducted in a double Cs corrected JEOL JEM-ARM200F (S)TEM with a cold-field emission gun operated at 80 kV, 10 µA. Physisorption measurements were carried out using a Quantachrome Quadrasorb SI apparatus with nitrogen sorption measurements at 77 K. The specific surface area of the sample was determined from the nitrogen adsorption data (P/P$_0$ < 0.2) using the Brunauer–Emmett–Teller (BET) method. The pore size distribution was determined using a quenched solid density functional theory (QSDFT) model with a slit/cylindrical pore shape using nitrogen adsorption data.

In Situ Electrochemical Liquid Cell TEM Experiments: A suspension of 6 mg mL^{-1} N-PHCSs in NMP with 10 wt.% PVDF was sonicated for 10 min before drop casting on the glassy carbon electrochemical chip purchased from Protochips (Protochips Inc.). The chip had one glassy carbon electrode patterned on the electron-transparent window region while one ring-shaped platinum electrode around the carbon electrode. The other small platinum electrode located away from the center which could be used as a reference electrode if needed. Glass capillaries (model 1B100-4, World Precision Instruments Inc.) were pulled into micropipettes using a pipette puller (model P-97, Sutter Instruments, Novato, CA.). Micropipette tips were cut using microforge (MF-900, Narishige, Tokyo, Japan. model) to obtain tips with an outer diameter of 50 µm. In order to load nanoparticles on the specific electrode patterned on the electrochemical chip, the Eppendorf FemtoJet apparatus was employed. Nanoparticle suspension (5 µL) was loaded into the glass capillary using Microloader tips. Thus, a loaded glass micropipette was fitted to the FemtoJet apparatus. Under the microscope, the tip of the glass micropipette was positioned above the injection zone of the chip. With an injection pressure (pi) of 15 hPa and injection time (ti) of 0.1 s (with zero compensation pressure (pc)), site-specific dropcasting N-PHCSs suspension was site-specifically drop-casted on the working electrode. The chip was then dried in vacuum at 60 °C for 12 h and stored in an Ar-filled glovebox. Sodium deposition was conducted in a homemade glass cell with two clamps connected to a piece of metallic sodium and the big Pt electrode on a drop-casted chip (Figure S11, Supporting Information). The Pt electrode was connected as the working electrode and metallic sodium as the counter and reference electrode. The negative current of 1 µA was applied for 300 s for depositing sodium on the Pt, following the method described in the previous article.[73] The chip with N-PHCSs loaded on the carbon electrode over the window region and sodium deposited on the surrounding ring electrode was mounted together with a 0 nm spacer chip using a liquid flow cell TEM holder with electrical biasing capabilities (Poseidon, Protochips Inc.).Electrolyte (5 µL) was directly dropped on the spacer chip with a pipette in the glovebox before sealing. Then sealed liquid cell TEM holder was inserted into a double Cs corrected JEOL JEM-ARM200F (S)TEM at 200 kV, 10 µA for an in situ experiment after leak checking on a turbo-pumped station (Pfeiffer Hi-cube 80Eco). Sequential HAADF-STEM images at a magnification of ×100K were taken with an acquisition time of 4 µs pixel^{-1} and an interval beam-blank time of 10 s to reduce the electron beam effect. In this case, the time resolution of the image series was 1/14 frame s^{-1}. The continuous acquisition at a lower magnification of ×40K was conducted to get a higher time resolution of 0.25 frame s^{-1}. Repeat chronopotentiometry with a constant current of 2 nA was applied for cycling N-PHCSs in the microcell while imaging in the TEM using a Gamery reference 600+ Potentiostat/Galvanostat/ZRA device with shielded cell cable (Gamry Instruments, Inc.).

Supporting Information

Supporting Information is available from the Wiley Online Library or from the author.

Acknowledgements

**ADVANCED
SCIENCE NEWS**

www.advancedsciencenews.com

**NANO · MICRO
small**

www.small-journal.com

Conflict of Interest

The authors declare no conflict of interest.

Data Availability Statement

Keywords

[1] M. Li, J. Lu, Z. Chen, K. Amine, *Adv. Mater.* **2018**, *30*, 1800561.

[2] Y. Wang, R. Chen, T. Chen, H. Lv, G. Zhu, L. Ma, C. Wang, Z. Jin, J. Liu, *Energy Storage Mater.* **2016**, *4*, 103.

[3] H. Zhao, J. Xu, D. Yin, Y. Du, *Chem. – A Eur. J.* **2018**, *24*, 18220.

[4] S. W. Kim, D. H. Seo, X. Ma, G. Ceder, K. Kang, *Adv. Energy Mater.* **2012**, *2*, 710.

[5] C. Vaalma, D. Buchholz, M. Weil, S. Passerini, *Nat. Rev. Mater.* **2018**, *3*, 18013.

[6] P. K. Nayak, L. Yang, W. Brehm, P. Adelhelm, *Angew. Chem., Int. Ed.* **2018**, *57*, 102.

[7] M. Sawicki, L. L. Shaw, *RSC Adv.* **2015**, *5*, 53129.

[8] K. Chayambuka, G. Mulder, D. L. Danilov, P. H. L. Notten, *Adv. Energy Mater.* **2018**, *8*, 1800079.

[9] J. Y. Hwang, S. T. Myung, Y. K. Sun, *Chem. Soc. Rev.* **2017**, *46*, 3529.

[10] P. Ge, M. Fouletier, *Solid State Ionics* **1988**, *28–30*, 1172.

[11] J. Sangster, *J Phase Equilibria Diffus* **2007**, *28*, 571.

[12] R. A. Adams, A. Varma, V. G. Pol, *Adv. Energy Mater.* **2019**, *9*, 1900550.

[13] H. Zhang, Y. Huang, H. Ming, G. Cao, W. Zhang, J. Ming, R. Chen, *J. Mater. Chem. A* **2020**, *8*, 1604.

[14] S. Zhao, Z. Guo, J. Yang, C. Wang, B. Sun, G. Wang, *Small* **2021**, *17*, 2007431.

[15] F. Xie, Z. Xu, Z. Guo, M.-M. Titirici, *Prog. Energy* **2020**, *2*, 042002.

[16] F. Su, X. S. Zhao, Y. Wang, L. Wang, J. Y. Lee, *J. Mater. Chem.* **2006**, *16*, 4413.

[17] D. Ni, W. Sun, Z. Wang, Y. Bai, H. Lei, X. Lai, K. Sun, *Adv. Energy Mater.* **2019**, *9*, 1900036.

[18] K. Schutjajew, J. Pampel, W. Zhang, M. Antonietti, M. Oschatz, *Small* **2021**, *17*, 2006767.

[19] K. Tang, L. Fu, R. J. White, L. Yu, M.-M. Titirici, M. Antonietti, J. Maier, *Adv. Energy Mater.* **2012**, *2*, 873.

[20] D. Li, H. Chen, G. Liu, M. Wei, L. X. Ding, S. Wang, H. Wang, *Carbon N Y* **2015**, *94*, 888.

[21] W. Ye, F. Pei, X. Lan, Y. Cheng, X. Fang, Q. Zhang, N. Zheng, D. L. Peng, M. S. Wang, *Adv. Energy Mater.* **2020**, *10*.

[22] M. Yuan, B. Cao, H. Liu, C. Meng, J. Wu, S. Zhang, A. Li, X. Chen, H. Song, *Chem. Mater.* **2022**, *34*, 3489.

[23] K. Schutjajew, T. Tichter, J. Schneider, M. Antonietti, C. Roth, M. Oschatz, *Phys. Chem. Chem. Phys.* **2021**, *23*, 11488.

[24] C. Bommier, T. W. Surta, M. Dolgos, X. Ji, *Nano Lett.* **2015**, *15*, 5888.

[25] H. Au, H. Alptekin, A. C. S. Jensen, E. Olsson, C. A. O'Keefe, T. Smith, M. Crespo-Ribadeneyra, T. F. Headen, C. P. Grey, Q. Cai, A. J. Drew, M. M. Titirici, *Energy Environ. Sci.* **2020**, *13*, 3469.

[26] N. Sun, J. Qiu, B. Xu, *Adv. Energy Mater.* **2022**.

[27] D. A. Stevens, J. R. Dahn, *J. Electrochem. Soc.* **2000**, *147*, 1271.

[28] Y. Cao, L. Xiao, M. L. Sushko, W. Wang, B. Schwenzer, J. Xiao, Z. Nie, L. V. Saraf, Z. Yang, J. Liu, *Nano Lett.* **2012**, *12*, 3783.

[29] Z. Tian, Y. Zhang, J. Zhu, Q. Li, T. Liu, M. Antonietti, *Adv. Energy Mater.* **2021**, *11*, 2102489.

[30] S. Qiu, L. Xiao, M. L. Sushko, K. S. Han, Y. Shao, M. Yan, X. Liang, L. Mai, J. Feng, Y. Cao, X. Ai, H. Yang, J. Liu, *Adv. Energy Mater.* **2017**, *7*, 1700403.

[31] W. Ren, Z. Zheng, C. Xu, C. Niu, Q. Wei, Q. An, K. Zhao, M. Yan, M. Qin, L. Mai, *Nano Energy* **2016**, *25*, 145.

[32] D. Wang, X. Bie, Q. Fu, D. Dixon, N. Bramnik, Y. S. Hu, F. Fauth, Y. Wei, H. Ehrenberg, G. Chen, F. Du, *Nat. Commun.* **2017**, *8*, 15888.

[33] Q. Gan, N. Qin, S. Gu, Z. Wang, Z. Li, K. Liao, K. Zhang, L. Lu, Z. Xu, Z. Lu, *Small Methods* **2021**, *5*, 2100580.

[34] S. D. Lacey, J. Wan, A. V. W. Cresce, S. M. Russell, J. Dai, W. Bao, K. Xu, L. Hu, *Nano Lett.* **2015**, *15*, 1018.

[35] D. Lin, K. Li, L. Zhou, *Etoiles Compos. Chim. Anorm. Debut Sequence Princ., Commun. Colloq. Int. Astrophys., 23rd* **2021**, *25*, 100635.

[36] H. Alptekin, H. Au, A. C. Jensen, E. Olsson, M. Goktas, T. F. Headen, P. Adelhelm, Q. Cai, A. J. Drew, M. M. Titirici, *ACS Appl. Energy Mater.* **2020**, *3*, 9918.

[37] L. Yao, P. Zou, L. Su, Y. Wu, Y. Pan, R. Fu, H. Min, L. Zhong, H. L. Xin, L. Sun, F. Xu, *Nano Energy* **2021**, *87*, 106182.

[38] Z. L. Wang, P. Poncharal, W. A. De Heer, *J. Phys. Chem. Solids* **2000**, *61*, 1025.

[39] P. Gao, Y. Y. Zhang, L. Wang, S. Chen, Y. Huang, X. Ma, K. Liu, D. Yu, *Nano Energy* **2017**, *32*, 302.

[40] J. Wan, F. Shen, W. Luo, L. Zhou, J. Dai, X. Han, W. Bao, Y. Xu, J. Panagiotopoulos, X. Fan, D. Urban, A. Nie, R. Shahbazian-Yassar, L. Hu, *Chem. Mater.* **2016**, *28*, 6528.

[41] H. Yang, L. W. Chen, F. He, J. Zhang, Y. Feng, L. Zhao, B. Wang, L. He, Q. Zhang, Y. Yu, *Nano Lett.* **2020**, *20*, 758.

[42] Z. Yi, Q. Tang, T. Jiang, Y. Cheng, *Nanotechnol Rev* **2019**, *8*, 266.

[43] T. Liu, L. Lin, X. Bi, L. Tian, K. Yang, J. Liu, M. Li, Z. Chen, J. Lu, K. Amine, K. Xu, F. Pan, *Nat. Nanotechnol.* **2019**, *14*, 50.

[44] X. F. Guo, Z. Yang, Y. F. Zhu, X. H. Liu, X. X. He, L. Li, Y. Qiao, S. L. Chou, *Small Methods* **2022**, *6*, 2200209.

[45] N. J. Gimble, L. A. Kraynak, J. D. Schneider, M. C. Schulze, A. L. Prieto, *J. Power Sources* **2021**, *489*, 229171.

[46] S. Komaba, W. Murata, T. Ishikawa, N. Yabuuchi, T. Ozeki, T. Nakayama, A. Ogata, K. Gotoh, K. Fujiwara, *Adv. Funct. Mater.* **2011**, *21*, 3859.

[47] B. Zhang, C. M. Ghimbeu, C. Laberty, C. Vix-Guterl, J. M. Tarascon, *Adv. Energy Mater.* **2016**, *6*, 1501588.

[48] C. Bao, B. Wang, Y. Xie, R. Song, Y. Jiang, Y. Ning, F. Wang, T. Ruan, D. Wang, Y. Zhou, *ACS Sustainable Chem. Eng.* **2020**, *8*, 5452.

[49] F. Xu, Y. Qiu, H. Han, G. Jiang, R. Zhao, E. Zhang, H. Li, H. Wang, S. Kaskel, *Carbon N Y* **2020**, *159*, 140.

[50] A. Agrawal, S. Janakiraman, K. Biswas, A. Venimadhav, S. K. Srivastava, S. Ghosh, *Electrochim. Acta* **2019**, *317*, 164.

[51] K. Gotoh, T. Yamakami, I. Nishimura, H. Kometani, H. Ando, K. Hashi, T. Shimizu, H. Ishida, *J. Mater. Chem. A* **2020**, *8*, 14472.

[52] Y. Morikawa, S. ichi Nishimura, R. ichi Hashimoto, M. Ohnuma, A. Yamada, *Adv. Energy Mater.* **2020**, *10*, 1903176.

[53] J. Fondard, E. Irisarri, C. Courrèges, M. R. Palacin, A. Ponrouch, R. Dedryvère, *J. Electrochem. Soc.* **2020**, *167*, 070526.

[54] S. Y. Lee, J. Shangguan, J. Shangguan, J. Alvarado, S. Betzler, S. J. Harris, M. M. Doeff, H. Zheng, *Energy Environ. Sci.* **2020**, *13*, 1832.

[55] O. S. Burheim, in *Engineering Energy Storage*, 1st ed., Academic Publisher, Cambridge, MA, USA **2017**, p. 75.

[56] T. Liu, L. Zhang, W. You, J. Yu, *Small* **2018**, *14*, 1702407.

[57] D. Yao, D. Wang, K. Hassan-Legault, A. Li, Y. Zhao, J. Lv, S. Huang, X. Ma, *ACS Catal.* **2019**, *9*, 2969.

[58] Y. J. Kim, Y. Horie, S. Ozaki, Y. Matsuzawa, H. Suezaki, C. Kim, N. Miyashita, M. Endo, *Carbon N Y* **2004**, *42*, 1491.

**ADVANCED
SCIENCE NEWS**

www.advancedsciencenews.com

**NANO · MICRO
small**

www.small-journal.com

[59] Z. Zeng, X. Zhang, K. Bustillo, K. Niu, C. Gammer, J. Xu, H. Zheng, *Nano Lett.* **2015**, *15*, 5214.

[60] L. Chen, R. Yan, M. Oschatz, L. Jiang, M. Antonietti, K. Xiao, *Angew. Chemie., Int. Ed.* **2020**, *59*, 9067.

[61] R. E. A. Ardhi, G. Liu, J. K. Lee, *ACS Energy Lett.* **2021**, 1432.

[62] X. H. Li, M. Antonietti, *Chem. Soc. Rev.* **2013**, *42*, 6593.

[63] Z. Wang, X. Feng, Y. Bai, H. Yang, R. Dong, X. Wang, H. Xu, Q. Wang, H. Li, H. Gao, C. Wu, *Adv. Energy Mater.* **2021**, 11.

[64] J. D. Lee, *Concise Inorganic Chemistry*, 4th ed., Chapman & Hall, London New York **1991**.

[65] D. T. Boyle, S. C. Kim, S. T. Oyakhire, R. A. Vilá, Z. Huang, P. Sayavong, J. Qin, Z. Bao, Y. Cui, *J. Am. Chem. Soc.* **2022**.

[66] K. Gotoh, *Batteries Supercaps* **2021**, *4*, 1267.

[67] M. E. Holtz, Y. Yu, D. Gunceler, J. Gao, R. Sundararaman, K. A. Schwarz, T. A. Arias, H. D. Abruña, D. A. Muller, *Microsc. Microanal.* **2014**, *20*, 1524.

[68] H. D. Asfaw, C. W. Tai, M. Valvo, R. Younesi, *Mater. Today Energy* **2020**, *18*, 100505.

[69] H. Daniels, R. Brydson, B. Rand, A. Brown, *Philos. Mag.* **2007**, *87*, 4073.

[70] C. Kunz, *Phys. Lett.* **1965**, *15*, 312.

[71] N. Jiang, D. Su, J. C. H. Spence, S. Zhou, J. Qiu, *J. Mater. Res.* **2008**, *23*, 2467.

[72] G. H. Kim, S. Jeong, *Sci. Rep.* **2015**, *5*, 11227.

[73] J. Hou, R. Girod, N. Nianias, T.-H. Shen, J. Fan, V. Tileli, *J. Electrochem. Soc.* **2020**, *167*, 110515.

2301415 (13 of 13)